

Synergistic inhibition of metastatic breast cancer by dual-chemotherapy with excipient-free rhein/DOX nanodispersions

Ruoning Wang^{1,2,†}, *Yujie Yang*^{1,2,†}, *Mengmeng Yang*^{1,2}, *Dandan Yuan*¹,

Jinyu Huang^{1,2}, *Rui Chen*¹, *Honglan Wang*^{1,2}, *Lihong Hu*^{1,3}, *Liuqing Di*^{1,2},

Junsong Li^{1,2,*}

1 School of Pharmacy, Nanjing University of Chinese Medicine, Nanjing, China

2 Jiangsu Engineering Research Center for Efficient Delivery System of TCM, Nanjing, China

3 Jiangsu Key Laboratory for Functional Substance of Chinese Medicine, Nanjing, China

† Contributed equally to this work.

Corresponding authors: Junsong Li

E-mail: lijunsong1964@163.com

Postal address: School of Pharmacy, Nanjing University of Chinese Medicine, 138

Xianlin Avenue, Nanjing 210023, China

Abstract

Background: The treatment of metastatic cancer continues to be very challenging worldwide. Notably, excipient-free nanodispersions that are entirely composed of pharmaceutically active molecules are regarded as promising candidates for the next generation of drug formulations. These molecules are mainly formulated from the self-assembly of drug molecules that enable the safe and effective delivery of therapeutic drugs to local diseased lesions. Herein, we developed a novel and green approach for preparing nanoparticles via the self-assembly of rhein (RHE) and doxorubicin (DOX) molecules, named RHE/DOX nanoparticles (RD NPs); this assembly was associated with π - π stacking interactions and did not involve any organic solvents.

Results: Molecular dynamics (MD) simulations showed that DOX molecules tend to assemble around RHE molecules through intermolecular forces. With the advantage of nanosizing, RD NPs improved the intracellular drug retention of DOX. As a dual-drug-loaded nanoformulation, the toxicity of RD NPs to tumor cells *in vitro* was synergistically enhanced. The combination of DOX and RHE in nanoparticles exhibited a synergistic effect with a combination index (CI) value of 0.51 and showed a stronger ability to induce cell apoptosis compared to that of free DOX. Furthermore, RD NPs treatment not only effectively suppressed primary tumor growth but also successfully inhibited tumor metastasis both *in vitro* and *in vivo*, with a good safety profile.

Conclusion: The generation of pure nanodrugs via a self-assembly approach might be an option and may provide inspiration for the fabrication of new excipient-free nanodispersions, especially for two small molecular antitumor drugs that could potentially have synergistic antiproliferation effects against metastatic breast cancer.

Keywords: Metastatic cancer; Synergistic antiproliferation; Rhein (RHE) and doxorubicin (DOX); Excipient-free nanodispersions

Background

The American Cancer Society and the National Cancer Institute assessed that there are more than 3.8 million women in the United States suffered with invasive breast cancer. Nearly 25% of these cases succumb to their disease resulted from the progression and development of distant metastases in the lungs etc. During the process of metastasis, tumor cells move systemically, and arrest at other organ; this process results in poor prognosis and increases the patients mortality [1-3]. The therapy for metastatic breast cancer mainly consists of chemotherapy [4,5]. Once metastases have developed, single-agent chemotherapy always fails to offer a durable response, ultimately leading to the death of patients [6].

Taking the limited clinical efficacy of single-agent chemotherapy for consideration, the combination of two or more drugs with aiming at different anticancer pathways has attracted the attention for improving anticancer effect at safe level during the treatment of metastatic cancer [7,8]. Over the past few decades, combination chemotherapy has shown superior efficacy compared with single-drug therapy. Nevertheless, owing to the distinctive pharmacokinetics of each agent, the effective drug dosage and ratio at the target tissue of conventional cocktail administrations are difficult to control [9,10]. Moreover, unexpected side effects of cocktail combinations have been reported in clinical trials [11]. Thus, the efficient co-delivery of multiple therapeutic agents to a target tissue with a controlled dose ratio and synergistic efficacy is highly desirable for future clinical translation. To address this need, many nanosized co-delivery architectures, such as liposomes [12], micelles [13,14], mesoporous silica nanoparticles

[15] and hydrogel [16], have been reported. For instance, the all-in-one brush-arm star polymer nanoparticles (NPs) were designed by ring-opening metathesis polymerization, which could generate precise molar ratios of doxorubicin (DOX), camptothecin and cisplatin. liposomes coloaded with oxaliplatin and irinotecan were developed that achieved synchronized delivery and exhibited superior antitumor activity compared to the free drugs. Despite these advancements, most of these methods require a large quantity of materials and involve complicated processes [17].

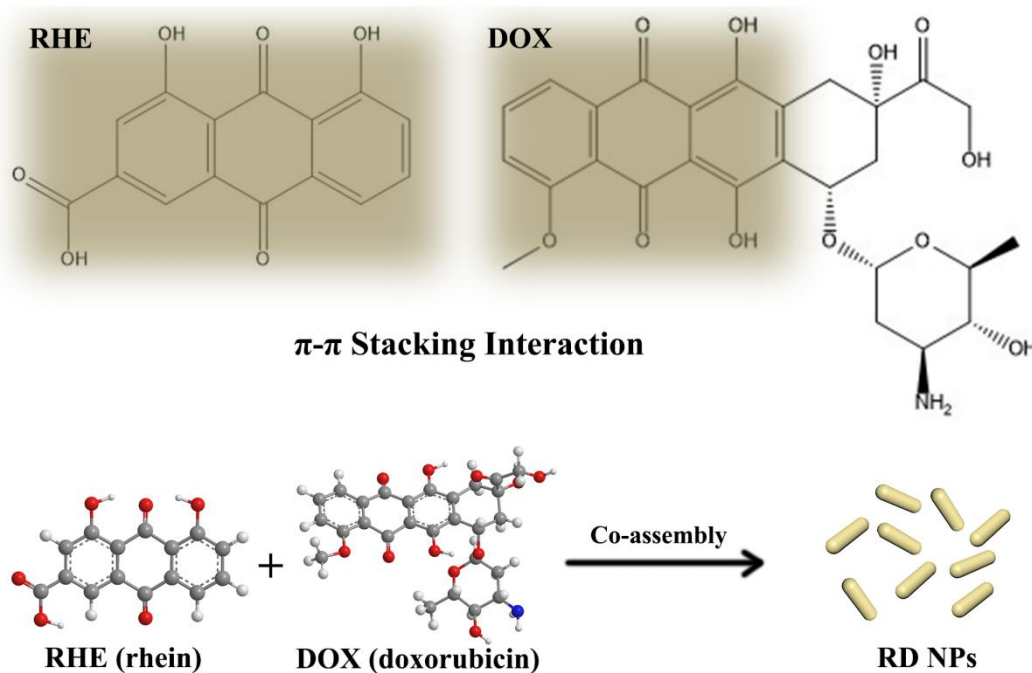
Up to now, though the great quantity of nanomedicine drug delivery systems were reported, only a few have been used in clinical. One major disadvantage for clinical usage is that current nanomedicines are always applying new materials or chemical modifications to agents [18-20]. The intensive clinical trials and final FDA approvals should be needed for these materials as excipients. Moreover, production of nanomedicines is often too complicated to develop scaling up manufacturing processes [21,22]. Therefore, it is necessary to design a “green” approach to design nanomedicines without “toxic” excipients. Nano-assembly strategy for designing excipient-free nanodispersions can be applied to nanoparticulate anticancer agents for enhancing therapeutic effects, which is the purpose of green pharmaceuticals [23,24]. Formulations and processes can be developed to eliminate the use and generate hazardous substances significantly [25]. Recently, the carrier-free dual-drug delivery system generated by the self-nanocrystallization of drugs was developed [1]. With DOX as a stabilizing agent, spherically assembled particles with a uniform size were prepared, and the water solubility of 10-hydroxycamptothecin (HCPT) was enhanced.

Furthermore, HCPT combined with the photosensitizer chlorin e6 was used as a stabilizer to obtain stable rod-like nanoparticles by using a nanoprecipitation method. However, studies have mainly focused on improving the solubility of drugs with poor solubility and have ignored its compatibility. Therefore, excipient-free “pure” nanodrugs could become next-generation nanomedicine [26].

DOX is widely used for solid tumors therapy, such as breast, lung and ovarian cancer; this compound enters cells by diffusing across the plasma membrane, entering the nucleus and causing DNA damage [19,23,27]. DOX further suppresses p53, bcl2, bax and caspase 3, leading to apoptosis of cancer cell [28]. Nevertheless, DOX also causes toxicity in the liver, kidney and heart. Meanwhile, the damaging effects of DOX to the cardiac muscle are cumulative and irreversible, which restricted the use of DOX [29,30]. Rhein (RHE), the bioactive molecules derived from the herb rhubarb, exhibits potent anti-inflammatory and antioxidant activity, which is safe even at high doses. The anticancer mechanisms of RHE include blocking the transcriptional factor NF- κ B, targeting the MAPK and p-AKT pathways. However, since RHE is a hydrophobic drug, vascular administration would be very difficult [13].

The structure of DOX is as surfactant, with unsaturated anthracycline rings and a saturated end of the ring system, acting as the hydrophobic part of the molecule or the hydrophilic properties, respectively, and abundant hydroxyl groups adjacent to the amino sugar. While, RHE is hydrophobic. Thus, DOX could potentially be designed to solubilize and nanosize RHE [23]. Meanwhile, the anticancer effect of DOX is restricted by the activation of the NF- κ B pathway, which plays a causal role in the

migration and invasion of tumor cells by positively regulating target genes. While, RHE can inhibit the expression of MMP-9 by suppressing the transcriptional activities of NF- κ B, thus inhibiting the migration and invasion. Therefore, the combination of DOX and RHE is predicted to have a synergistic effect during the treatment of metastatic cancer [4]. The novel and green approach to excipient-free nanodispersions is developed by using the self-assembly of RHE and DOX molecules that was associated with π - π stacking interactions and did not involve any organic solvents (Scheme 1). The simultaneous formation of RHE/DOX nanoparticles (RD NPs) can be resulted from the strong interaction forces between RHE and DOX. DOX has the same parent aromatic part as RHE, therefore the strong π - π stacking forces between in them to form a hydrophobic core, and the hydrophilic daunosamine heads of DOX stick out, making the nanoparticle dispersible.



Scheme 1 Schematic representation of RD NPs preparation via the co-assembly of RHE and DOX,

which was associated with π - π stacking interactions.

Experimental section

Materials

DOX and RHE were obtained from Shanghai Yuanye Biological Technology Co., Ltd. (Shanghai, China). MTT was purchased from Fluka (MO, USA). The Annexin V-FITC Kit was purchased by Nanjing Jiancheng Bioengineering Institute (Nanjing, China). All other reagents or chemicals used were of an analytical reagent grade and their purity was confirmed before use.

Molecular dynamics (MD)

Classical MD simulations were carried out by employing the AMBER16 package [31,32]. The force field parameters for DOX and RHE molecules were obtained from the generalized Amber force field (GAFF). The atomic charges were generated with the restrained electrostatic potential (RESP) method [33,34]. An artificial box containing 8 DOX, 8 RHE and 2000 water molecules was generated by using the leap module in Amber Tools. The periodic boundary conditions were used, with the long-range electrostatic interactions computed with the particle-mesh Ewald summation. The SHAKE algorithm was used to constrain the bonds involving hydrogen atoms that did not stretch. The cutoff value for the nonbonded interactions was 8.0 Å. The system was optimized for 2500 steps with the steepest descent method followed by 2500 steps with the conjugate gradient method. Then, the system was heated from 0 K to 300 K

gradually under the NVT ensemble for 200 ps. Finally, the MD trajectory was accumulated for 12 ns under the NPT ensemble (300 K and 1 atm) [21].

Preparations of nanoparticles

The RD NPs were developed with a “green self-assembly approach” [9.35]. Briefly, 3 mL of water was heated, and 30 μ L of RHE (20 mM) was added under ultrasonication (ultrasonic cleaner, KH-500DE, 300 W). Then, 60 μ L DOX (10 mM) was added, and the resulting sample was ultrasonicated for 1 h. After removing the free RHE and DOX in nanoparticles by an ultrafiltration method, the RD NPs were ready for further use. Other formulations with various molar ratios (feeding ratio) of RHE to DOX were prepared as mentioned above.

To prepare the mixture of RHE and DOX (RHE/DOX), an equal volume of solution of RHE (2 mg/mL) in 40% polyethylene glycol (PEG 400) (containing 5% NaHCO₃, m/v) and aqueous DOX solution (2 mg/mL) were mixed.

Characterizations of nanoparticles

The diameter and zeta potential of RD NPs were characterized by dynamic light scattering (DLS) using a Malvern Zeta-sizer (NanoZS90, Malvern Instruments Ltd., UK). Transmission electron microscope (TEM) detections were performed by a Zeiss EM 912 Omega TEM. Fluorescence spectrometer (Hitachi F-4500) was applied to acquire the spectrum of free RHE, free DOX and RD NPs. The concentration of RHE and DOX in the nanoparticles was determined by HPLC method (Waters Alliance 2695

System, Milford, America). For chromatography, a KromasiL C18 column, acetonitrile/sodium dodecyl sulfate solution, and a 254 nm detection wavelength were used [19,27]. The encapsulation efficiency (EE) was detected by an ultrafiltration approach. The free drug in the filtrate was detected, and the EE was measured by the equation:

$$EE (\%) = (\text{total drug} - \text{free drug}) / \text{total drug} \times 100 \quad (1)$$

The storage stability of RD NPs was evaluated at 4 °C. The diameter and polydispersity index (PDI) were detected at predetermined time intervals. For serum stability study, RD NPs were incubated with fetal bovine serum (FBS) at a volume ratio of 2:1. The diameter and PDI were analyzed at designated time intervals (0, 1, 2, 4, 8, 12, and 24 h).

Drug release test

A dialysis method was applied to detect the *in vitro* release profile [2,20]. RHE, DOX and RD NPs were sealed in dialysis bags (3500 Da) and immersed in phosphate-buffered saline (PBS) solutions (pH 7.4 or 5.0). The tubes were gently shaken in water bath. At specific time intervals, 1 mL of the external buffer was withdrawn and immediately replaced with 1 mL fresh media, and the release amounts of RHE and DOX were analyzed using HPLC, as mentioned above. All the experiments were operated in triplicate.

Cell culture

The mouse breast cancer cell line 4T1 was obtained from Shanghai Institute of Biochemistry and Cell Biology (Shanghai, China). 4T1 cells were incubated in Dulbecco's modified Eagle's medium (DMEM) in the atmosphere containing 5% CO₂ at 37 °C.

Cellular uptake analysis

Ten thousand 4T1 cells were seeded for confocal laser scanning microscopy (CLSM, Carl Zeiss AG, Germany). The cells were treated with RHE, DOX, RHE/DOX and RD NPs (2 μM RHE and 1 μM DOX) for 4 h. Cells were visualized with CLSM. RHE was excited at the wavelength of 360 nm, and DOX was at 475 nm [8,36].

***In vitro* cytotoxicity assay**

The cytotoxicity of RHE, DOX, RHE/DOX and RD NPs against 4T1 cells was evaluated in MTT assays [2,18]. Briefly, cells were seeded and cultured. Then, increased concentrations of RHE, DOX, RHE/DOX and RD NPs (5, 10, 20, 50 and 100 μM RHE; and 0.2, 0.4, 1, 2 and 5 μM DOX) were added to the medium of each well. After incubating for 48 h, MTT was added. Then, the absorbance was measured at 490 nm by a microplate reader. The cell viability was measured by the equation:

$$\text{Cell viability (\%)} = \text{O.D.}_{(\text{sample})} / \text{O.D.}_{(\text{control})} \times 100 \quad (2)$$

The combination index (CI) of RHE and DOX was analyzed by Chou–Talalay equation [10]:

$$\text{CI}_x = (D)_1 / (D_x)_1 + (D)_2 / (D_x)_2 \quad (3)$$

D_x represents the required dose of RHE or DOX for an $x\%$ inhibition rate, and $(D)_1$ and $(D)_2$ stand for the doses of RHE and DOX, respectively, which could achieve the inhibition effect in combination at same level. CI values less than 1 indicate synergism, CI values equal to 1 indicate an additive effect, while CI values greater than 1 represents the antagonistic effect.

Apoptosis assay

Apoptosis in 4T1 cells exposed to RHE, DOX, RHE/DOX and RD NPs was measured in annexin-propidium iodide assays. The cells were treated with RHE, DOX, RHE/DOX and RD NPs (RHE-equivalent dose of 2 μM or a DOX-equivalent dose of 1 μM). The cells were collected and stained with annexin V-FITC/PI double staining after 48 h incubation. Cellular apoptosis was quantitatively determined by flow cytometry. The 4T1 cells without any treatment were set as control.

Wound healing assay

After the 4T1 cells (1.5×10^5 cells per well) formed a confluent monolayer, the monolayer was scratched for producing a gap. Then, cells were incubated with RHE, DOX, RHE/DOX and RD NPs at a concentration equal to 2 μM of RHE and 1 μM of DOX for 48 h. The obtained images, which were photographed of the wound healing areas with the microscope, were performed by ImageJ to quantify. While, the areas detected at 48 h were normalized to the initial areas to determine the relative migration rates [24,37].

***In vitro* migration and invasion**

4T1 cells (5×10^3 cells per well) were added to the upper chambers of Transwell inserts. The cells were then treated with RHE, DOX, RHE/DOX and RD NPs (equal to 2 μ M of RHE and 1 μ M of DOX) and were treated for 48 h. As for the invasion assays, 4T1 cells (5×10^3 cells per well) were added to the upper chambers, which were coated with Matrigel. The cells were then treated with the drugs (equal to 2 μ M of RHE and 1 μ M of DOX) and were incubated for 48 h. Cells that passed through the membrane on the lower surface were stained with crystal violet, then were quantified by a microplate reader [3,37].

Western blot analysis of cells

4T1 cells were treated with RHE, DOX, RHE/DOX and RD NPs (2 μ M RHE and 1 μ M DOX) for 48 h. Total cell proteins were extracted by a protein extraction kit. The concentration of protein was measured by a bicinchoninic protein assay. After blocking step, the membrane was incubated with a primary antibody against NF- κ B p65, MMP-9, Bcl-2, Bax or β -actin (Wuhan Servicebio Technology Co., Ltd, China; diluted at 1:300) overnight, then the membrane was incubated with a secondary antibody. The resulting bands were observed by an ECL-plus detection system [23].

Animals

Female BALB/c mice (18-22 g) and male Sprague Dawley (SD) rats (180-220 g) were

purchased from Shanghai Laboratory Animal Center (Shanghai, China). Animal assays were carried on accordance with the Guidelines for Animal Experimentation of Nanjing University of Chinese Medicine, and the protocol was approved by the institution's Animal Ethics Committee.

To establish an orthotopic 4T1 tumor-bearing mouse model, 4T1 cells were suspended and injected into the right inguinal mammary fat pad of the mice [38,39]. Tumor volume (V) was assessed by measuring the length (a) and width (b) by a caliper, then determined by the following equation:

$$V = a \times b^2/2. \quad (4)$$

Pharmacokinetic and biodistribution analysis

For pharmacokinetic analysis, SD rats (n=6) were administered RHE, DOX, RHE/DOX and RD NPs at the RHE dose of 5 mg/kg and DOX dose of 5 mg/kg via tail vein injection. At 0.083, 0.167, 0.25, 0.5, 1, 2, 4, 6, 8, 12 and 24 h post injection, 500 μ L of blood was collected, which was centrifuged to obtain the plasma. Plasma samples (100 μ L) were mixed with 500 μ L of ethyl acetate, 10 μ L of 5 μ g/mL ibuprofen and 0.5 μ g/mL daunorubicin (used as internal standards for RHE and DOX), and 10 μ L of 10% acetic acid. The mixture was vortexed and then centrifuged. The organic layer was evaporated until dry under a nitrogen stream and was reconstituted with methanol. An aliquot (10 μ L) was subjected to ultra-performance liquid chromatography-tandem mass spectrometry (UPLC-MS/MS) analysis [37].

When the tumor size reached approximately 500 mm³, 4T1 tumor-bearing mice

were intravenously injected with DOX and RD NPs (5 mg/kg of DOX). For *ex vivo* imaging, the mice were sacrificed at 12 and 24 h post injection. The main tissues were harvested and immediately imaged after sacrifice with an *in vivo* imaging system on the DOX channel. The semiquantitative biodistribution analysis of the average fluorescence intensity was determined by Image Lab Software. Additionally, the harvested tumors were frozen and sectioned, then observed by CLSM.

For the biodistribution analysis, 4T1 tumor-bearing mice were injected with RHE, DOX, RHE/DOX and RD NPs at RHE dose of 5 mg/kg and a DOX dose of 5 mg/kg (3 mice at each time point per group). At 12 and 24 h after administration, the mice were sacrificed and main tissues were harvested. The tissue samples were weighed and homogenized, then the samples were processed and analyzed [9,40].

***In vivo* antitumor efficacy**

BALB/c mice bearing 4T1 tumors were randomly divided into 5 groups (n=5) when the tumor size reached approximately 100 mm³. Animals were treated saline, RHE, DOX, RHE/DOX and RD NPs (RHE at 5 mg/kg and DOX at 5 mg/kg) every other day via *i.v.*. The tumor size and body weight were observed every other day, and the tumor inhibition rate (TIR) was measured by the equation:

$$\text{TIR (\%)} = \frac{(\text{Tumor weight}_{(\text{control group})} - \text{tumor weight}_{(\text{sample group}))}{\text{tumor weight}_{(\text{control group})}} \times 100. \quad (5)$$

The tumors were harvested and operated for pathological analysis (hematoxylin and eosin (H&E) and TUNEL detection), when the mice were sacrificed on day 12.

Each of the five pulmonary lobes was separated, and tumors on the surface were calculated. Then the lungs were sectioned and stained with H&E [41].

Immunohistochemical analysis

The expression of NF- κ B P65, MMP-9, Bcl-2 and Bax was analyzed in tumor tissues by immunohistochemical staining. Tumor tissues were sectioned and deparaffinized by EZ-Dewax. The paraffin sections were first nonspecifically blocked. Then sections were treated with primary antibodies. After incubating with avidin-biotin complex, the immunoreactivity was visualized [2,35,42].

Western blot analysis of tissues

For the western blot assay, tissues were homogenized. The total protein content was determined by a BCA protein assay kit. After blocking, the membranes were treated with primary antibodies against NF- κ B P65, MMP-9, Bcl-2, Bax and β -actin. Then the membranes were treated with a secondary antibody. Then, the membranes were observed by an imaging system, and the densitometry of the bands was analyzed with Image Pro-plus.

Safety profiles

BALB/c mice were injected with saline, DOX and RD NPs (DOX at 5 mg/kg) every other day. On day 12, blood was collected and analyzed by the blood analyzer and autoanalyzer. The major organs were harvested for H&E analysis [5].

Statistical analysis

All the data are presented as the means \pm the standard deviation (SD). Comparisons between groups were analyzed by one-way analysis of variance, followed by a Student's t-test. Significant differences are indicated as $*p < 0.05$, $**p < 0.01$, or $***p < 0.001$.

Results and discussion

Molecular dynamics (MD)

MD simulations were operated for RHE and DOX to help understand how the molecules interact with each other in aqueous solutions. The RHE and DOX molecules were initially in a dispersed state. After 2 ns, they spontaneously clustered, and the assembly phenomena emerged; then clusters gradually gathered closer to each other and became ordered. A stable aggregation was ultimately formed within 11 ns (Additional file 1: Figure S1). The assembly was mainly stabilized by π - π stacking interactions, in which the distances between the RHE and DOX moieties were 3.6–3.7 Å (Fig. 1).

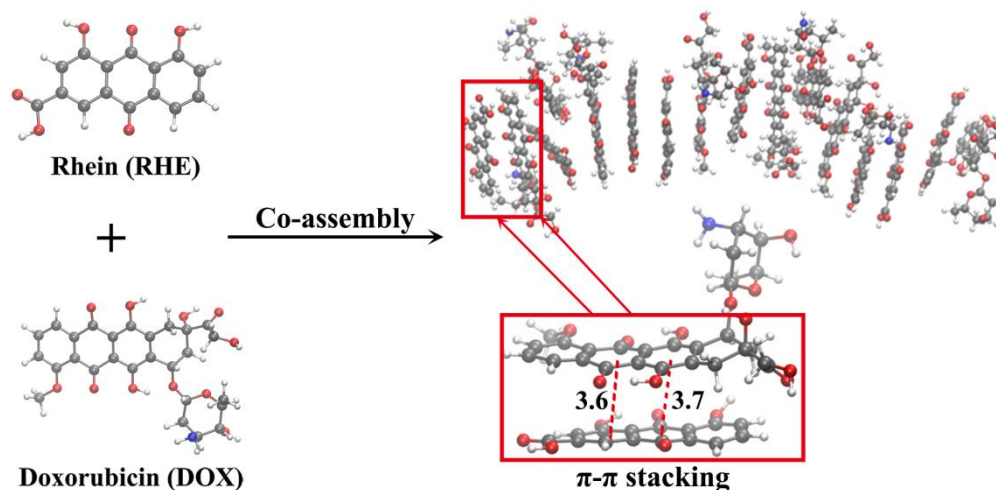


Fig. 1 MD simulations of the co-assembly of RHE and DOX molecules in water after 11 ns. The representative position of the noncovalent interaction is indicated by arrows. The magnified graph shows representative structures and the distance between the interacting moieties, which displayed π - π interactions.

Preparation and characterization of RD NPs

The assembled RHE particles formed irregular sheet-like structures, which were characterized by TEM (Fig. 2A). When the DOX was added to the RHE suspension (RHE/DOX molar ratio = 1:1), DOX molecules co-assembled with RHE via π - π stacking interactions and formed rod-like RD NPs with diameters of approximately 240 nm, which was also confirmed by MD simulations (Fig. 2B and S2). The DOX in aqueous solution was clear and transparent, and the solution of RD NPs showed obvious Tyndall light scattering (Fig. 2D). The DLS analysis of RD NPs demonstrated a narrow monomodal distribution, with a small mean hydrodynamic diameter of 249.90 ± 5.20 nm and a PDI of 0.14 ± 0.03 , which was within the accepted range for efficient EPR and ensured passive tumor targeting effect. The surface charge of RD NPs was determined to be 25.67 ± 1.03 mV (Additional file 1: Figure S3). The EE of RHE and

DOX were $96.23 \pm 0.22\%$ and $50.98 \pm 7.72\%$, respectively (Table 1). Furthermore, the emission intensity of RD NPs was found to be lower than that of the DOX aqueous solution due to the aggregation induced by the π - π stacking interactions (Fig. 2C). RD NPs showed an increased emission intensity compared to that of RHE, indicating that the aggregation of RHE is partly inhibited by the interactions between RHE and DOX. This may be attributed to the encapsulation of RHE in the hydrophobic domains of DOX.

Table 1. The Encapsulation Efficiency (EE) of RHE and DOX in their self-assembled nanoparticles (NPs).

Molar ratio	RHE (%)	DOX (%)
RHE/DOX=1:0.5	98.29 ± 0.58	70.26 ± 3.47
RHE/DOX=1:1	96.23 ± 0.22	50.98 ± 7.72
RHE/DOX=1:2	94.14 ± 2.51	30.54 ± 5.81

Colloid stability plays the important role in the biomedical application of nanoscale drug-delivery systems. There were no significant changes in the hydrodynamic diameter together with the PDI of RD NPs for up to 8 days (Fig. 2E). Additionally, the co-assembled NPs retained good colloidal stability in 10% FBS (Fig. 2F). Although no surfactants or excipients were applied, the RD NPs displayed desirable stability without any precipitation and phase separation.

RHE, DOX, and RD NPs were dispersed in buffer solutions with pH 7.4 and 5.0 to test the release profile at 37 °C for 24 h. In Fig. 2G and H, there was no significant difference in the release properties for free RHE and DOX in different pH, and the drugs

were released almost 80% during the first 2 h. By contrast, the release rate was slower in the RD NPs group than that in the free RHE and DOX solutions. Nearly 25% of RHE and 20% of DOX were released from RD NPs (pH = 7.4) in 2 h. While, RD NPs in the PBS solution (pH = 5.0), the release rate of DOX slightly increased, while that of RHE slowed. A total of $73.95 \pm 8.93\%$ of RHE and $92.07 \pm 1.78\%$ of DOX was released from NPs at pH 5.0 during 24 h; both release rates would improve the effect of therapy. The relatively slower RHE release rate might result from the carboxyl groups of RHE, which are more readily protonated in acidic conditions, decreasing its solubility and decelerating its diffusion. Similarly, the slightly faster release of DOX can be due to the increased solubility associated with the protonated amino group in acidic conditions [43].

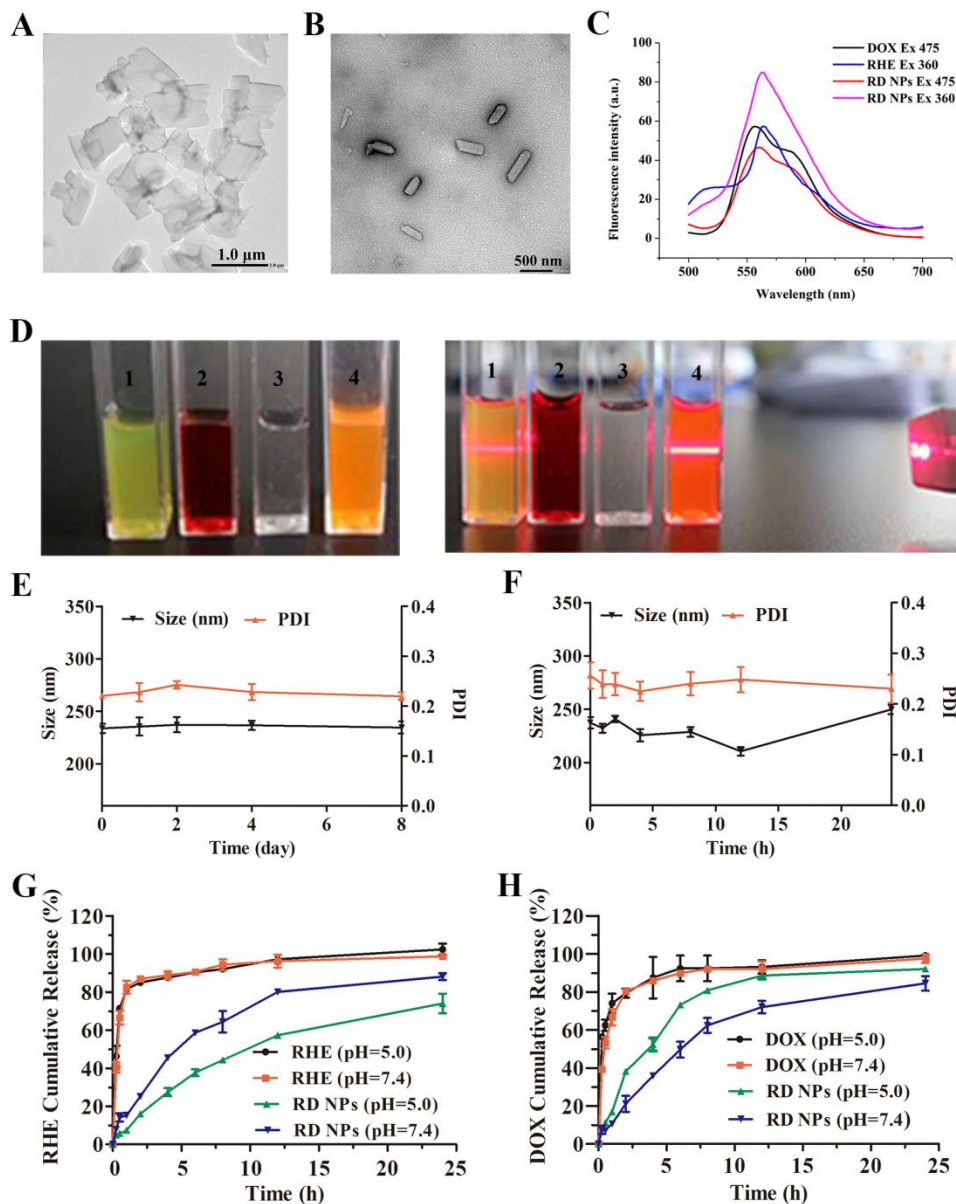


Fig. 2 (A) TEM image of RHE. (B) TEM image of RD NPs. (C) Fluorescence spectra of RHE (200 μM), DOX (200 μM) and RD NPs (200 μM RHE and 200 μM DOX). The λ_{ex} (RHE) = 360 nm; λ_{ex} (DOX) = 475 nm. (D) Photographs and the Tyndall effect of 1) RHE in a DMSO/water solution (99% water), 2) DOX in aqueous solution, 3) H_2O , and 4) RD NPs in a DMSO/water solution (99% water). (E) The particle size and PDI of RD NPs during storage at 4 $^\circ\text{C}$. (F) Changes in the particle size and PDI of RD NPs stored in 10% FBS for 24 h. Cumulative release of (G) RHE and (H) DOX from RHE, DOX and RD NPs at pH 7.4 and 5.0.

Cellular uptake analysis

To verify whether RD NPs could be efficiently internalized by cancer cells, we compared the cellular uptake effect of RHE, DOX, RHE/DOX and RD NPs in human breast cancer 4T1 cells. According to CLSM images (Fig. 3A), RD NPs noticeably increased the cellular uptake of RHE and DOX, leading to much more green and red fluorescence intensity in 4T1 cells compared with that in the free RHE, free DOX and RHE/DOX groups. These data were also qualitatively corroborated by the line-scanning profiles of fluorescence intensity over selected cells (Fig. 3B). The green and red lines represent RHE and DOX fluorescence intensity, respectively. The fluorescence intensity of RHE and DOX in the RD NPs was much higher than that of the RHE, DOX or RHE/DOX groups, and the colocalization of red and green fluorescence showed that DOX and RHE could be co-delivered to the cells. The enhanced accumulation of these drugs in 4T1 cells mediated by the nanosuspension was expected to improve their antitumor effect.

***In vitro* antitumor efficacy**

To evaluate the antitumor efficiency of RD NPs, the *in vitro* cytotoxicity of RHE, DOX, RHE/DOX and RD NPs was assessed by MTT assays in 4T1 cells. As shown in Fig. 3C, D and E, there were dose-dependent effects of all the formulations on 4T1 cells. Free RHE and free DOX had an IC_{50} of 73.86 ± 4.40 and 1.30 ± 0.22 μ M, respectively (Table 2). Compared with the single-drug treatments, combination therapy with RHE and DOX caused relatively lower cell viability. The IC_{50} of DOX was reduced to 0.84 ± 0.16 μ M, combining with RHE in the mixture. Furthermore, the cell viability in RD

NPs group was further reduced, with an IC_{50} of $0.63 \pm 0.23 \mu\text{M}$. The increased antitumor efficacy of RD NPs could be attributed to several factors. RHE and DOX were simultaneously internalized in the cells, which allowed both drugs to support each other's individual antitumor effects. In addition, RD NPs were taken up more efficiently by cells than free drugs. In addition, we calculated the CI values of RHE/DOX and RD NPs. As shown in Table 2, the CI value of RHE/DOX was 0.68, demonstrating a strong synergistic antiproliferative efficacy. Moreover, it was noteworthy that the RD NPs had a CI value of 0.51; therefore, the relatively profound synergistic efficacy of RD NPs was consistent with the cytotoxicity results.

Table 2. The IC_{50} against 4T1 cells of RHE/DOX and RD NPs.

Samples	IC_{50} (μM)	
	RHE	DOX
RHE	73.86 ± 4.40	-
DOX	-	1.30 ± 0.22
RHE/DOX	2.53 ± 0.43	0.84 ± 0.16
RD NPs	1.88 ± 0.60	0.63 ± 0.23

Apoptosis refers to programmed cell death controlled by genes that maintain the stability of the internal milieu. The rate of apoptosis is a significant index for evaluating the therapeutic effect mediated by antineoplastic agents. We measured the apoptosis induced by RD NPs through double staining with annexin V-FITC and PI. As displayed in Fig. 3F, RHE/DOX and RD NPs showed a stronger ability to induce cell apoptosis ($31.30 \pm 4.69\%$ and $37.40 \pm 5.88\%$) than free DOX ($21.27 \pm 2.08\%$). Meanwhile, the

RD NPs group induced an even higher level of apoptosis than the RHE/DOX group, which can probably be due to the enhanced cellular uptake of the NPs compared to that of the free drugs.

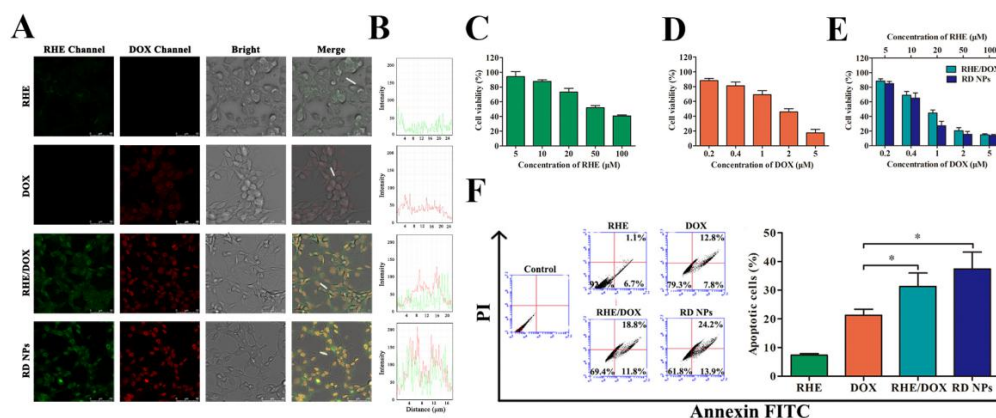


Fig. 3 (A) Cellular uptake of RHE, DOX, RHE/DOX and RD NPs at the equivalent RHE concentration (2.0 µM) and DOX concentration (1.0 µM) in 4T1 cells observed by CLSM. (B) Line-scanning profiles of the fluorescence intensity of 4T1 cells that were incubated with these preparations. *In vitro* cytotoxicity of 4T1 cells treated with (C) RHE, (D) DOX, (E) RHE/DOX and RD NPs for 48 h. (F) Cell apoptosis study in 4T1 cells after incubation with RHE, DOX, RHE/DOX and RD NPs. (n = 3, mean ± SD). **p* < 0.05.

***In vitro* anti-metastatic effects**

The ability of RD NPs to inhibit the metastasis of 4T1 cells *in vitro* was detected. A wound healing assay was applied to investigating cell migration, and the images of wound healing that preincubated with various formulations were evaluated after scratching to evaluate the inhibitory effect of RD NPs on cell migration (Fig. 4A). As displayed in Fig. 4A and B, the wound healing rates of RHE, DOX, RHE/DOX and RD NPs were $39.64 \pm 5.84\%$, $53.66 \pm 2.57\%$, $35.29 \pm 3.22\%$ and $28.32 \pm 3.84\%$, respectively. Thus, RHE/DOX and RD NPs exerted a stronger inhibitory effect on the

wound healing rate than DOX. The migration and invasion detection (Fig. 4E) were performed to further determine the inhibitory effects of RHE, DOX, RHE/DOX and RD NPs on 4T1 cell migration. As exhibited in Fig. 4C and F, the cells treated with RHE, DOX, RHE/DOX and RD NPs exhibited a decreased migration ability compared to the control, with migration rates of $53.05 \pm 8.47\%$, $61.22 \pm 2.08\%$, $47.42 \pm 3.21\%$ and $40.08 \pm 8.54\%$, respectively, indicating that RHE/DOX and RD NPs exhibited the stronger inhibitory effect on migration than free DOX. Furthermore, the results of the invasion assay were consistent with the data obtained from the wound healing and migration detections (Fig. 4D and G). The inhibition of cell migration by RHE/DOX and RD NPs could be attributed to the downregulation of the NF- κ B protein, which is an essential part of metastasis process.

NF- κ B is a critical part in the progression of cell migration, invasion and proliferation; thus, the NF- κ B gene is relative important in cell metastasis and apoptosis. Therefore, the expression of a variety of proteins, including NF- κ B P65, the metastasis-related protein MMP-9, the proapoptotic protein Bax and the antiapoptotic protein Bcl-2, were analyzed via western blot after treatment with RD NPs to detect the mechanism cell migration inhibition of RHE/DOX and RD NPs. As shown in Fig. 4H and I, following treatment with RHE/DOX or RD NPs, the expression levels of NF- κ B P65 and MMP-9 were significantly decreased when compared those with DOX treatment alone ($p < 0.01$). Furthermore, when taking the DOX group as comparison, the RD NPs group had significantly decreased Bcl-2 levels ($p < 0.001$). In addition, Bax expression significantly increased in the RHE/DOX and DOX groups ($p < 0.01$). These data

demonstrated that the inhibition of NF- κ B P65 was an anti-metastasis and apoptosis mechanism in response to the combination of RHE and DOX. Moreover, the RD NPs group had the lowest expression level of NF- κ B P65 due to the enhanced cellular uptake of the NPs in this group compared to that of the drugs in the other groups.

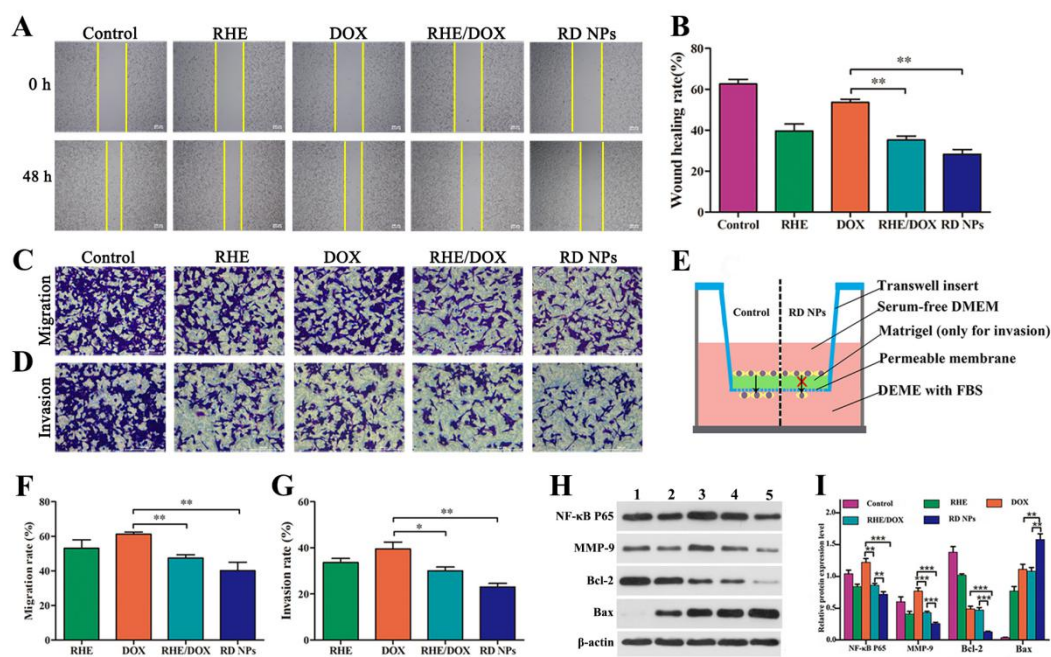


Fig. 4 (A) The wound healing images and (B) quantitative analysis 48 h after scratching. Microscopy images of (C) migration and (D) invasion and the quantitative analysis (F, G) of 4T1 cells that passed through the membrane after incubation with RHE, DOX, RHE/DOX and RD NPs compared with the control group (nontreated cells). (E) Schematic diagram of 4T1 cell migration and invasion in the Transwell insert. (H) Protein expression of NF- κ B P65, MMP-9, Bcl-2 and Bax in 4T1 cells, as determined by western blot analysis. Lane 1: blank; Lane 2: RHE; Lane 3: DOX; Lane 4: RHE/DOX; and Lane 5: RD NPs. (I) The bar diagrams show the relative band intensities of NF- κ B P65, MMP-9, Bcl-2 and Bax. ($n = 3$, mean \pm SD). ** $p < 0.01$, *** $p < 0.001$.

Pharmacokinetic and biodistribution analysis

As shown in Fig. 5A, RD NPs exhibited higher blood circulation levels when comparing to RHE, DOX and RHE/DOX after intravenous (*i.v.*) injection. The

concentrations of free RHE, free DOX or RHE/DOX decreased rapidly in 12 h, while RD NPs exhibited significantly delayed blood clearance. The analysis of the pharmacokinetic parameters demonstrated that RD NPs increased the half-life of RHE from 1.81 h to 6.87 h (Table 3). Similarly, the RD NPs extended the half-life of DOX from 2.92 h to 7.14 h. In addition, the area under the curve ($AUC_{0-\infty}$) of RHE increased by ~11.36-fold for RD NPs compared to that of free RHE. Similarly, the $AUC_{0-\infty}$ of DOX increased by ~9.44-fold for RD NPs compared to that of free DOX. These results indicated that RD NPs showed improved pharmacokinetic profiles and might have superior synergistic antitumor efficacy *in vivo*.

Table 3. Main pharmacokinetic parameters of drugs in rats after intravenous injection of different drugs (n = 5).

Drugs	Formulations	C_{\max} ($\mu\text{g/mL}$)	$T_{1/2}$ (h)	$AUC_{0-\infty}$ (mg/mL·h)	CL (L/h/kg)	$MRT_{0-\infty}$ (h)
	Free RHE	0.35±0.10***	1.81±0.57*	0.94±0.52***	6.25±2.65*	2.51±0.98
RHE	RHE/DOX	0.62±0.29***	2.15±0.10*	1.25±0.52***	4.49±1.86*	2.59±1.07
	RD NPs	5.46±0.92	6.87±2.11	10.68±1.04	0.47±0.04	5.20±2.31
	Free DOX	0.36±0.04*	2.92±0.14*	1.59±0.06*	3.15±0.12***	5.07±0.29*
DOX	RHE/DOX	0.52±0.07	3.21±0.05*	1.61±0.15*	3.11±0.30***	5.24±0.60*
	RD NPs	2.09±0.48	7.14±1.42	15.01±5.55	0.37±0.14	9.63±2.33

* $p < 0.05$, ** $p < 0.01$, *** $p < 0.001$, compared to RD NPs.

Encouraged by the enhanced therapeutic efficiency of RD NPs *in vitro*, the biodistribution of RD NPs was detected by fluorescence imaging. Since the DOX

fluorescence was weak *in vivo*, the mice were euthanized, and tissues (heart, liver, spleen, lung, kidney and tumor) were excised to carry out *ex vivo* imaging, which was more accurate for the qualitative biodistribution analysis. As shown in Fig. 5C and D, the quantitative region-of-interest analysis of DOX fluorescence *ex vivo* substantiated the superior tumor accumulation ability of RD NPs, as higher DOX intensity was observed in tumor, with levels 1.68- and 3.38-fold higher than those of free DOX at 12 and 24 h, respectively. The intra-tumoral distribution of DOX was also observed in frozen tissue sections at 24 h post-injection (Fig. 5E), which showed that treatment with RD NPs led to higher DOX intensity in tumor than free DOX treatment. The drastically higher accumulation of RD NPs was probably due to the long-term circulation and the EPR effect of the NPs.

The fluorescence of DOX was used to observe the biodistribution of nanoparticles *in vivo*. To more intuitively and accurately observe the accumulation of DOX and RHE, we conducted biodistribution experiments and performed quantitative analysis. To evaluate the tumor accumulation of RHE and DOX, biodistribution assays were performed with RHE, DOX and RD NPs. Free RHE had lower accumulation in tumor tissues than RD NPs (Additional file 1: Figure S4). Similarly, free DOX and RHE/DOX had lower DOX accumulation in tumor tissues than RD NPs. Moreover, the RHE accumulation in tumors via RD NPs was 1.45- fold higher than that of free RHE at 24 h post-injection. Similarly, the DOX of RD NPs accumulated in the tumors was 3.42-fold higher than that of free DOX at 24 h post-injection. In addition, the highest DOX concentration of RD NPs ($10.94 \pm 0.91 \mu\text{g/g}$) at the tumors site was reached at 12 h,

consistent with the data from the isolated tumor imaging. Accordingly, it was confirmed that RD NPs had high tumor accumulation than the free drugs. These results demonstrated that RD NPs were efficiently delivered to the tumor via EPR effects. We also observed that RD NPs caused low DOX accumulation in the heart [14]. However, few NPs accumulated in other organs. This is a common biological challenge, as most NPs become rapidly sequestered from the blood, following by their accumulation in the reticuloendothelial system (RES) organs, like the spleen or lung [44].

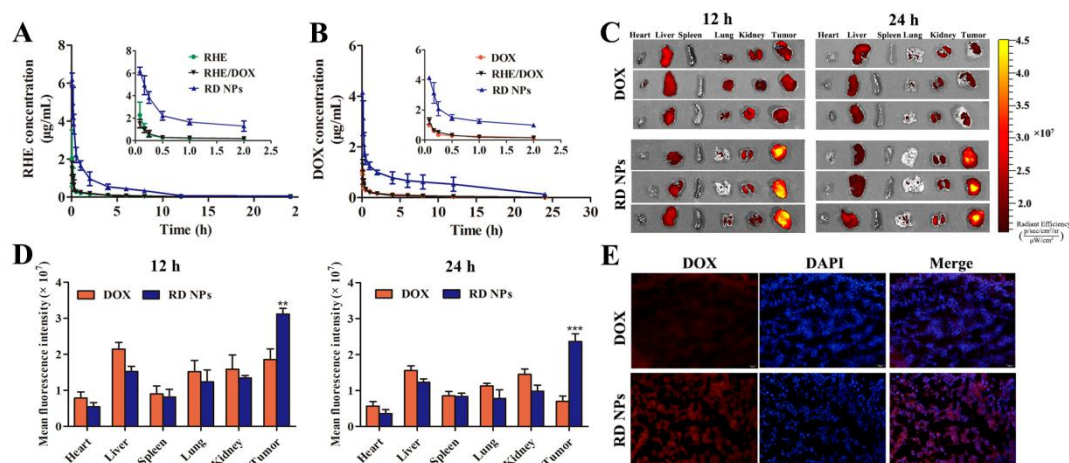


Fig. 5 (A) The plasma RHE concentration-time curve of injected RHE, RHE/DOX and RD NPs ($n = 6$, mean \pm SD). (B) The plasma DOX concentration-time curve of injected DOX, RHE/DOX and RD NPs ($n = 6$, mean \pm SD). (C) *Ex vivo* images of tumors and major organs at 12 h and 24 h post-injection. (D) Semiquantitative analysis of the *ex vivo* DOX fluorescence intensity in the tumor and major organs at 12 h and 24 h post-injection ($n = 3$, mean \pm SD). $**p < 0.01$, $***p < 0.001$. (E) Confocal images of frozen tumor sections collected after 24 h. DOX is shown in red, and the nucleus is shown in blue (DAPI).

***In vivo* antitumor efficacy**

To evaluate the benefits of combination therapy with RD NPs, a metastatic orthotropic

4T1 mammary adenocarcinoma model was used. As displayed in Fig. 6A, rapid tumor growth was detected in the saline group, while moderately restricting tumor growth was observed when treating with DOX or RHE/DOX. Tumor growth was significantly inhibited in the RD NPs group, and the TIR was $55.90 \pm 2.58\%$ on day 10 (Fig. 6B), which was further confirmed by images of tumor xenografts in mice (Fig. 6C). The RD NPs group had the lowest tumor volume after the final injection, demonstrating that combining RHE and DOX had a synergistic antitumor effect [45]. The H&E staining of the tumor tissues harvested at the end of the study displayed the greatest cancer cell clearance in the RD NPs group, which included coagulative necrosis and empty intercellular spaces, further validating the high antitumor activity of this treatment. The TUNEL analysis demonstrated the highest level of induced cell apoptosis in this condition (Fig. 6D).

The orthotopic 4T1 model applied in this therapeutic study spontaneously forms lung metastases. We therefore evaluated whether RD NPs treatment had an antimetastatic effect. To assess the antimetastatic efficacy, photographs of lung metastases and the H&E staining of lung sections were examined. As shown in Fig. 6E and F, the RD NPs treatment led to the significantly decreased number of metastatic lesions on the lung surface compared to the control treatment. In addition, the analysis of the lung tissue sections further supported these results. Thus, the RD NPs not only effectively inhibited primary tumor growth but successfully suppressed tumor metastasis as well, which was consistent with the results showing *in vitro* antimetastatic effects [46].

Immunohistochemical analysis was used to detect whether tumor growth and aggressiveness was associated with NF- κ B downregulation (Fig. 6G). Excised tumor sections in the RHE/DOX or RD NP groups had lower NF- κ B P65 and MMP-9 protein expression than those in the DOX group. Additionally, the expression level of the proapoptotic protein Bax was the highest, while the expression level of the antiapoptotic protein Bcl-2 was the lowest, in RD NPs group. Taking comparison with free DOX, the efficient silencing of NF- κ B P65 and the enhanced apoptosis of RHE/DOX were probably due to the presence of RHE. The RD NPs likely caused the greatest downregulation of NF- κ B P65 and the highest apoptosis among the treatments because of the EPR effect in the RD NPs group. In addition, the improved pharmacokinetic profiles in the RD NPs group may have prolonged their circulation time and increased accumulation of the drugs in the tumor.

NF- κ B has been exhibited to play an important role in cancer cell migration and invasion. Thus, we investigated the effects of RD NPs on cell migration and invasion. The RD NPs treatment groups significantly inhibited cell migration compared to the DOX treatment group ($p < 0.001$). As displayed in Fig. 6H and I, MMP-9 expression, which regulates cell invasion, was reduced in the RD NPs treatment group compared with the DOX group ($p < 0.001$). These data demonstrated that the enhanced inhibition of cell migration and invasion was likely resulted from the greater inhibition of NF- κ B activity and the reduced expression of MMP-9. Additionally, the expression level of the proapoptotic protein Bax was maximized in the RD NPs group. Meanwhile, the minimized expression level of the antiapoptotic protein Bcl-2 was observed in the RD

NPs group. Therefore, the inhibition of NF- κ B or anti-NF- κ B therapy could apply as a possible therapeutic approach to control cancer metastasis. Therefore, the RD NPs would inhibit the metastatic breast cancer efficiently.

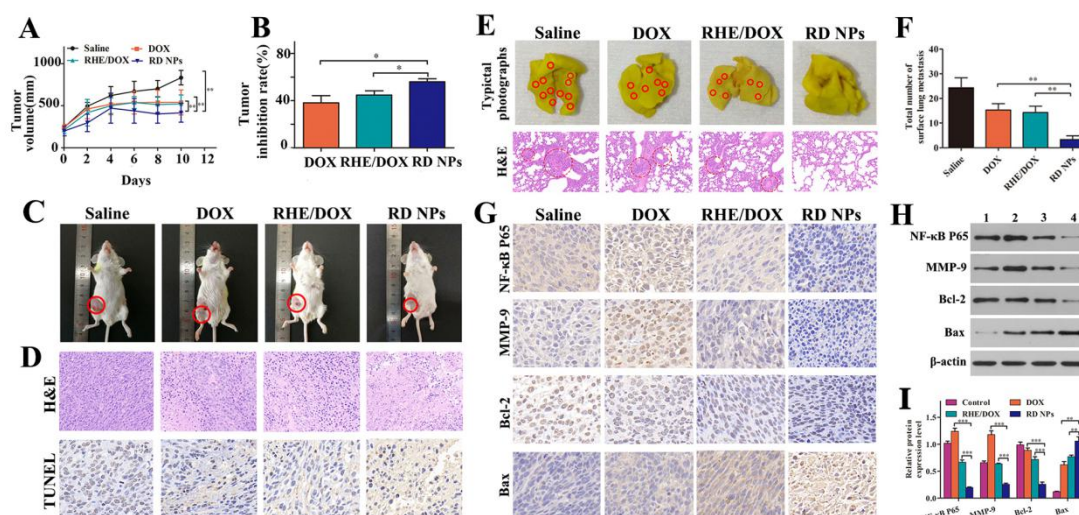


Fig. 6 (A) 4T1 tumor growth curves of the study groups ($n=5$, mean \pm SD), including saline, DOX, RHE/DOX and RD NPs with an equivalent DOX concentration of 5 mg/kg. (B) The tumor inhibition of the study groups ($n=5$, mean \pm SD). (C) Representative images of the tumor-bearing mice two days after the final treatment. (D) Histological comparison of the tumor tissues at the conclusion of the study. (E) Representative photographs of whole lungs from mice in different groups and H&E staining of lung tissue sections. Surface lung metastases are denoted by red circles. (F) Average number of surface lung metastases ($n=5$, mean \pm SD). (G) Immunohistochemical analysis of tumor tissues after tumor treatments in tissues that were stained for NF- κ B P65, MMP-9, Bcl-2 and Bax. (H) Protein expression of NF- κ B P65, MMP-9, Bcl-2 and Bax in tumors, as determined by western blot analysis. Lane 1: blank; Lane 2: DOX; Lane 3: RHE/DOX; and Lane 4: RD NPs. (I) The bar diagrams show the relative band intensities of NF- κ B P65, MMP-9, Bcl-2 and Bax. ($n = 3$, mean \pm SD). * $p < 0.05$, ** $p < 0.01$, *** $p < 0.001$.

Safety profiles

To evaluate whether RD NPs induced any adverse effects during treatment, body weight,

biochemical functions and histopathological changes were evaluated and compared, with saline and free DOX were set as the negative and positive control, respectively. None of the treatments led to severe body weight losses (Fig. 7A), indicating that no severe systemic toxicity caused by RD NPs. As shown in Fig. 7B, RD NPs had no measurable adverse effect on blood cells, as well as on the heart, liver and renal functions, based on the safety profiles. The peripheral blood cells were all within the normal range, indicating that no illnesses, including hemolytic anemia and acute infection. In the blood chemistry analysis, cardiac troponin I (cTnI), the liver function biomarkers, e.g., alanine aminotransferase (ALT), aminotransferase, total protein and albumin, and the renal function biomarkers, e.g., blood urea nitrogen (BUN), creatinine (CRE), glutamic acid and uric acid (UA), were all normal, indicating that the RD NPs had negligible hepatotoxicity and nephrotoxicity (Fig. 7C). In contrast, the levels of cTnI, ALT, BUN, CRE and UA were significantly increased in the free DOX group compared to those in the control group, indicating that there was acute inflammation in the heart, liver and kidney. The histopathological results also verified these conclusions (Fig. 7D). The mice did not exhibit the toxicity of the major organs in the RD NPs and saline group, while abnormal architecture was observed in the heart, liver and kidney tissues of animals pretreated with DOX, such as cavities in the heart, cytoplasmic degeneration of hepatocytes in the liver, and focal tubular necrosis in the kidney, indicating the apparent cardiotoxicity, hepatotoxicity and nephrotoxicity of DOX. In summary, these results demonstrated that RD NPs had superior therapeutic efficacy at safe level.

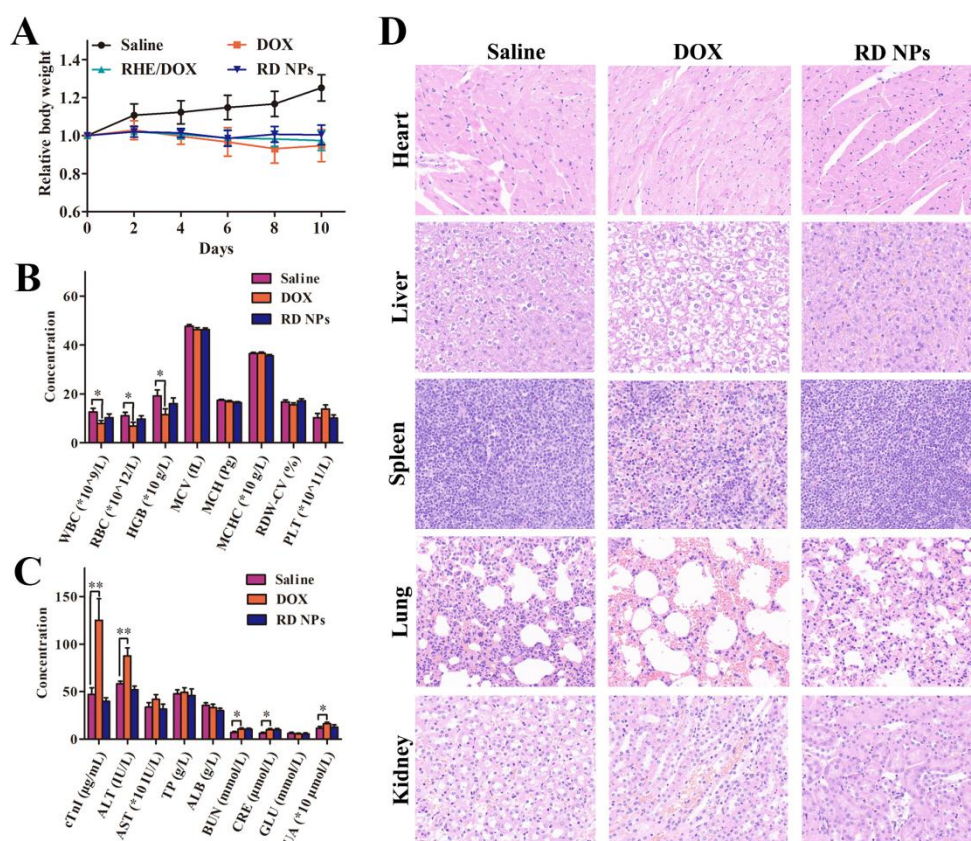


Fig. 7 (A) Body weight curve of mice bearing tumors generated from 4T1 cells. (B) Hematological and (C) blood biochemical analysis of the mice. (D) Histopathology of tissues from the saline, DOX, and RD NPs (n = 5, mean ± SD). * $p < 0.05$, ** $p < 0.01$.

Conclusions

Collectively, RHE was nanosized with the assistance of DOX to fabricate carrier-free RD NPs by the simple “green” preparation. RHE and DOX molecules tend to co-assemble via π - π stacking interactions and form rod-like morphology with satisfactory stability. Cellular uptake assays demonstrated that drug accumulation could be significantly enhanced after RD NPs treatment. Importantly, compared with free RHE, free DOX, and RHE/DOX, RD NPs demonstrated superior cytotoxicity against 4T1

cells resulted in the potent synergistic therapy via the nanodispersions. The synergistic effect mechanism research demonstrated that RHE can inhibit migration and invasion of tumor cells by suppressing the expression of NF- κ B and MMP-9. Taken together, the design of pure nanomedicine might create the novel approach and give inspiration to fabricate novel carrier-free nanodrugs for theranostics, especially for achieving the aim of combinational antitumor therapy in the synergistic way.

Supplementary material

Supplementary data associated with this article can be found in the online version at

Additional file 1: Figure S1. MD simulations of the co-assembly of RHE and DOX molecules in aqueous solution during 11 ns. **Figure S2.** The size of RD NPs. **Figure S3.** The zeta potential of RD NPs. **Figure S4.** Distribution of RHE from RHE group and RD NPs group in each tissue at 12 h (A) and 24 h (B) post injection. Distribution of DOX from DOX group and RD NPs group in each tissue at 12 h (C) and 24 h (D) post injection.

Abbreviations

RHE: rhein; DOX: doxorubicin; RD NPs: RHE/DOX nanoparticles; MD: Molecular dynamics; CI: combination index; HCPT: 10-hydroxycamptothecin; GAFF: the generalized Amber force field; RESP: the restrained electrostatic potential; RHE/DOX: RHE and DOX; DLS: dynamic light scattering; TEM: transmission electron microscope; EE: encapsulation efficiency; PDI: polydispersity index; FBS: fetal bovine serum; PBS: phosphate-buffered saline; DMEM: Dulbecco's modified Eagle's medium;

CLSM: confocal laser scanning microscopy; UPLC-MS/MS: ultra-performance liquid chromatography-tandem mass spectrometry; TIR: tumor inhibition rate; H&E: hematoxylin and eosin; $AUC_{0-\infty}$: the area under the curve; RES: reticuloendothelial system; cTnI: cardiac troponin I; ALT: alanine aminotransferase; BUN: blood urea nitrogen; CRE: creatinine; UA: uric acid.

Declarations

Ethics approval and consent to participate

Not applicable.

Consent for publication

All authors have provided consent for the manuscript to be published.

Availability of data and materials

All data generated or analyzed during this study are included in this published article.

Competing interests

The authors declare that they have no competing interests.

Funding

The authors acknowledge financial support from National Natural Science Foundation of China (No. 81903557), Natural Science Foundation of Jiangsu Province (No.

BK20190802), and Natural Science Foundation of the Jiangsu Higher Education Institutions of China (No.19KJB350003). This study was also supported by the Project Funded by the Priority Academic Program Development of Jiangsu Higher Education Institutions (PAPD).

Authors' contributions

Ruoning Wang and Junsong Li designed the experiments and organized the research. Yujie Yang, Mengmeng Yang, Dandan Yuan and Jinyu Huang performed the experiments and analyzed the data. The manuscript was written by Ruoning Wang and Yujie Yang. Ruoning Wang, Rui Chen, Honglan Wang, Lihong Hu, Liuqing Di, Junsong Li supervised the experiments and edited the final version of the manuscript. All authors read and approved the final manuscript.

Acknowledgements

Not applicable.

References

1. Kushwah V, Katiyar SS, Agrawal AK, Gupta RC, Jain S. Co-delivery of docetaxel and gemcitabine using PEGylated self-assembled stealth nanoparticles for improved breast cancer therapy. *Nanomedicine*. 2018;14(5):1629-41.
2. Dong QL, Zhang HQ, Han Y, Djamila A, Cheng H, Tang ZY, Zhou JP, Ding Y. Tumor environment differentiated "nanodepot" programmed for site-specific drug shuttling and combinative therapy on metastatic cancer. *J Controlled Release*. 2018;283:59-75.
3. Zhang ZW, Cao HQ, Jiang SJ, Liu ZY, He XY, Yu HY, Li, Y. Nanoassembly of probucol enables novel therapeutic efficacy in the suppression of lung metastasis of breast cancer. *Small*. 2014;10(22):4735-45.

4. Li J, Liang X, Zhang J, Yin YZ, Zuo TT, Wang YY, Yang XM, Shen Q. Inhibiting pulmonary metastasis of breast cancer based on dual-targeting graphene oxide with high stability and drug loading capacity. *Nanomedicine*. 2018;14(4):1237-48.
5. Jiang ZQ, Wang YJ, Sun L, Yuan B, Tian YC, Xiang LC, Li YY, Li Y, Li J, Wu AG. Dual ATP and pH responsive ZIF-90 nanosystem with favorable biocompatibility and facile post-modification improves therapeutic outcomes of triple negative breast cancer in vivo. *Biomaterials*. 2019;197:41-50.
6. Xiao QQ, Zhu X, Yuan YT, Yin LF, He W. A drug-delivering-drug strategy for combined treatment of metastatic breast cancer. *Nanomedicine*. 2018;14(8):2678-88.
7. Zhang JM, Li JJ, Shi Z, Yang Y, Xie X, Lee SM, Wang YT, Leong KW, Chen MW. pH-sensitive polymeric nanoparticles for co-delivery of doxorubicin and curcumin to treat cancer via enhanced pro-apoptotic and anti-angiogenic activities. *Acta Biomater*. 2017;58:349-64.
8. Hou BB, Yang WT, Dong CH, Zheng B, Zhang Y, Wu J, Wang HJ, Chang J. Controlled co-release of doxorubicin and reactive oxygen species for synergistic therapy by NIR remote-triggered nanoimpellers. *Mater Sci Eng C*. 2017;74:94-102.
9. Wang RN, Han Y, Sun B, Zhao ZQ, Opoku-Damoah Y, Cheng H, Zhang HQ, Zhou JP, Ding Y. Deep Tumor Penetrating Bioparticulates Inspired Burst Intracellular Drug Release for Precision Chemo-Phototherapy. *Small*. 2018;14(12):1703110.
10. Xiao YT, Liu J, Guo MY, Zhou HG, Jin J, Liu JM, Liu Y, Zhang ZJ, Chen CY. Synergistic combination chemotherapy using carrier-free celastrol and doxorubicin nanocrystals for overcoming drug resistance. *Nanoscale*. 2018;10(26):12639-49.
11. Shi CY, Guo DD, Xiao K, Wang X, Wang LL, Luo JT. A drug-specific nanocarrier design for efficient anticancer therapy. *Nat Commun*. 2015;6:7449.
12. Jia YL, Wang CC, Zheng JH, Lin GS, Ni DL, Shen ZW, Huang BX, Li Y, Guan JT, Hong WD, Chen YF, Wu RH. Novel nanomedicine with a chemical-exchange saturation transfer effect for breast cancer treatment in vivo. *J Nanobiotechnol*. 2019;17(1):123.
13. Han NN, Li X, Tao L, Zhou Q. Doxorubicin and rhein loaded nanomicelles attenuates multidrug resistance in human ovarian cancer. *Biochem. Biophys Res Commun*. 2018;498(1):178-85.
14. Yang T, Lan Y, Cao M, Ma XQ, Cao AC, Sun Y, Yang JH, Li L, Liu YH. Glycyrrhetic acid-conjugated polymeric prodrug micelles co-delivered with doxorubicin as combination therapy treatment for liver cancer. *Colloids Surf B*. 2019;175:106-15.
15. Gupta B, Poudel BK, Ruttala HB, Regmi S, Pathak S, Gautam M, Jin SG, Jeong JH, Choi HG, Ku SK, Yong CS, Kim JO. Hyaluronic acid-capped compact silica-supported mesoporous titania nanoparticles for ligand-directed delivery of doxorubicin. *Acta Biomater*. 2018;80:364-77.
16. Gao M, Yang YF, Bergfel A, Huang LL, Zheng L, Bowden TM. Self-assembly of cholesterol end-capped polymer micelles for controlled drug delivery. *J Nanobiotechnol*. 2020;18(1):13.
17. Han LQ, Wang TQ, Mu SJ, Yin XL, Liang S, Fang H, Liu YJ, Zhang N. Unified D- α -Tocopherol 5-Fu/SAHA bioconjugates self-assemble as complex nanodrug for optimized combination therapy. *Nanomedicine*. 2018;13(11):1285-301.
18. Ding Y, Han Y, Wang RN, Wang YZ, Chi C, Zhao ZQ, Zhang HQ, Wang W, Yin LF, Zhou JP. Rerouting Native HDL to Predetermined Receptors for Improved Tumor-Targeted Gene Silencing Therapy. *ACS Appl Mater Interfaces*. 2017;9(36):30488-501.
19. Maksimenko A, Dosio F, Mouglin J, Ferrero A, Wack S, Reddy LH, Weyn AA, Lepeltier E, Bourgaux C, Stella B, Cattel L, Couvreur P. A unique squalenoylated and nonpegylated doxorubicin

nanomedicine with systemic long-circulating properties and anticancer activity. *Proc Natl Acad Sci U. S. A.* 2014;111(2):E217-26.

20. Huang P, Wang DL, Su Y, Huang W, Zhou YF, Cui DX, Zhu XY, Yan DY. Combination of small molecule prodrug and nanodrug delivery: amphiphilic drug-drug conjugate for cancer therapy. *J Am Chem Soc.* 2014;136(33):11748-56.

21. Hu SQ, Lee E, Wang C, Wang JQ, Zhou ZX, Li YX, Li XY, Tang JB, Lee DH, Liu XR, Shen YQ. Amphiphilic drugs as surfactants to fabricate excipient-free stable nanodispersions of hydrophobic drugs for cancer chemotherapy. *J Controlled Release.* 2015;220(Pt A):175-9.

22. Wang JN, Tan JY, Luo JH, Huang PL, Zhou WY, Chen LM, Long LL, Zhang LM, Zhu BH, Yang LQ, Deng DYB. Enhancement of scutellarin oral delivery efficacy by vitamin B12-modified amphiphilic chitosan derivatives to treat type II diabetes induced-retinopathy. *J Nanobiotechnol.* 2017;15(1):18.

23. Asampille G, Verma BK, Swain M, Shettar A, Rosenzweig SA, Kondaiah P, Atreya HS. An ultra-stable redox-controlled self-assembling polypeptide nanotube for targeted imaging and therapy in cancer. *J Nanobiotechnol.* 2018;16(1):101.

24. Sun HP, Su JH, Meng QS, Yin Q, Zhang ZW, Yu HJ, Zhang PC, Wang SL, Li YP. Silibinin and indocyanine green-loaded nanoparticles inhibit the growth and metastasis of mammalian breast cancer cells in vitro. *Acta Pharmacol Sin.* 2016;37(7):941-9.

25. Wang RN, Gu XC, Zhou JP, Shen LJ, Yin LF, Hua PY, Ding Y. Green design "bioinspired disassembly-reassembly strategy" applied for improved tumor-targeted anticancer drug delivery. *J Controlled Release.* 2016;235:134-46.

26. Chen F, Zhao Y, Pan Y, Xue X, Zhang X, Kumar A, Liang XJ. Synergistically Enhanced Therapeutic Effect of a Carrier-Free HCPT/DOX Nanodrug on Breast Cancer Cells through Improved Cellular Drug Accumulation. *Mol Pharmaceutics.* 2015;12(7):2237-44.

27. Willerding L, Limmer S, Hossann M, Zengerle A, Wachholz K, Ten Hagen TLM, Koning GA, Sroka R, Lindner LH, Peller M. Method of hyperthermia and tumor size influence effectiveness of doxorubicin release from thermosensitive liposomes in experimental tumors. *J Controlled Release.* 2016;222:47-55.

28. Fan YP, Liao JZ, Lu YQ, Tian DA, Ye F, Zhao PX, Xiang GY, Tang WX, He XX. MiR-375 and Doxorubicin Co-delivered by Liposomes for Combination Therapy of Hepatocellular Carcinoma. *Mol Ther Nucleic Acids.* 2017;7:181-9.

29. Zhao PX, Wu SP, Cheng Y, You J, Chen Y, Li MS, He CC, Zhang XJ, Yang T, Lu Y, Lee RJ, He XX, Xiang GY. MiR-375 delivered by lipid-coated doxorubicin-calcium carbonate nanoparticles overcomes chemoresistance in hepatocellular carcinoma. *Nanomedicine.* 2017;13(8):2507-16.

30. Jiang X, Hong YQ, Zhao D, Meng XX, Zhao LJ, Du YW, Wang Z, Zheng Y, Cai L, Jiang HY. Low dose radiation prevents doxorubicin-induced cardiotoxicity. *Oncotarget.* 2018;9(1):332-45.

31. Case DA, Cheatham TE, Darden T, Gohlke H, Luo R, Merz KM, Onufriev A, Simmerling C, Wang B, Woods RJ. The Amber biomolecular simulation programs. *J Comput Chem.* 2005;26(16):1668-88.

32. Wang JM, Wolf RM, Caldwell JW, Kollman PA, Case DA. Development and testing of a general amber force field. *J Comput Chem.* 2004;25(9):1157-74.

33. Karnati KR, Wang YX. Understanding the co-loading and releasing of doxorubicin and paclitaxel using chitosan functionalized single-walled carbon nanotubes by molecular dynamics simulations. *Phys Chem Chem Phys.* 2018;20(14):9389-400.

34. Peng SY, Yuan XZ, Lin WJ, Cai CZ, Zhang LJ. pH-responsive controlled release of mesoporous silica nanoparticles capped with Schiff base copolymer gatekeepers: Experiment and molecular dynamics simulation. *Colloids Surf B*. 2019;176:394-403.
35. Han Y, Ding BX, Zhao ZQ, Zhang HQ, Sun B, Zhao YP, Jiang L, Zhou JP, Ding Y. Immune lipoprotein nanostructures inspired relay drug delivery for amplifying antitumor efficiency. *Biomaterials*. 2018;185:205-18.
36. Jiao J, Liu C, Li X, Liu J, Di DH, Zhang Y, Zhao QF, Wang SL. Fluorescent carbon dot modified mesoporous silica nanocarriers for redox-responsive controlled drug delivery and bioimaging. *J Colloid Interface Sci*. 2016;483:343-52.
37. Ji YJ, Xiao YY, Xu L, He JY, Qian C, Li WD, Wu L, Chen R, Wang JJ, Hu RF, Zhang XD, Gu Z, Chen ZP. Drug-Bearing Supramolecular MMP Inhibitor Nanofibers for Inhibition of Metastasis and Growth of Liver Cancer. *Adv Sci*. 2018;5(8):1700867.
38. Xie DP, Du JJ, Bao MY, Zhou AW, Tian CL, Xue LJ, Ju CY, Shen J, Zhang C. A one-pot modular assembly strategy for triple-play enhanced cytosolic siRNA delivery. *Biomater Sci*. 2019;7(3):901-13.
39. Saffholm A, Tuomela J, Rosenkvist J, Dejmek J, Harkonen P, Andersson T. The Wnt-5a-Derived Hexapeptide Foxy-5 Inhibits Breast Cancer Metastasis In vivo by Targeting Cell Motility. *Clin Cancer Res*. 2008;14(20):6556-63.
40. Qiao HZ, Fang D, Zhang L, Gu XC, Lu Y, Sun MJ, Sun CM, Ping QN, Li JS, Chen ZP, Chen J, Hu LH, Di LQ. Nanostructured Peptidotoxins as Natural Pro-Oxidants Induced Cancer Cell Death via Amplification of Oxidative Stress. *ACS Appl Mater Interfaces*. 2018;10(5):4569-81.
41. Wang YZ, Xie Y, Li J, Peng ZH, Sheinin Y, Zhou JP, Oupicky D. Tumor-Penetrating Nanoparticles for Enhanced Anticancer Activity of Combined Photodynamic and Hypoxia-Activated Therapy. *ACS Nano* 2017;11(2):2227-38.
42. Cheng PF, Han P, Zhao CL, Zhang SX, Wu HL, Ni JH, Hou P, Zhang YZ, Liu JY, Xu HD, Liu S, Zhang XN, Zheng YF, Chai YM. High-purity magnesium interference screws promote fibrocartilaginous entheses regeneration in the anterior cruciate ligament reconstruction rabbit model via accumulation of BMP-2 and VEGF. *Biomaterials*. 2016;81:14-26.
43. Chen W, Zhong P, Meng FH, Cheng R, Deng C, Feijen J, Zhong ZY. Redox and pH-responsive degradable micelles for dually activated intracellular anticancer drug release. *J Controlled Release*. 2013;169(3):171-9.
44. Hameed S, Bhattarai P, Liang XL, Zhang NS, Xu YX, Chen M, Dai ZF. Self-assembly of porphyrin-grafted lipid into nanoparticles encapsulating doxorubicin for synergistic chemophotodynamic therapy and fluorescence imaging. *Theranostics*. 2018;8(19):5501-18.
45. Shahin M, Soudy R, Aliabadi HM, Kneteman N, Kaur K, Lavasanifar A. Engineered breast tumor targeting peptide ligand modified liposomal doxorubicin and the effect of peptide density on anticancer activity. *Biomaterials*. 2013;34(16):4089-97.
46. Pei Q, Hu XL, Liu S, Li Y, Xie ZG, Jing XB. Paclitaxel dimers assembling nanomedicines for treatment of cervix carcinoma. *J Controlled Release*. 2017;254:23-33.